#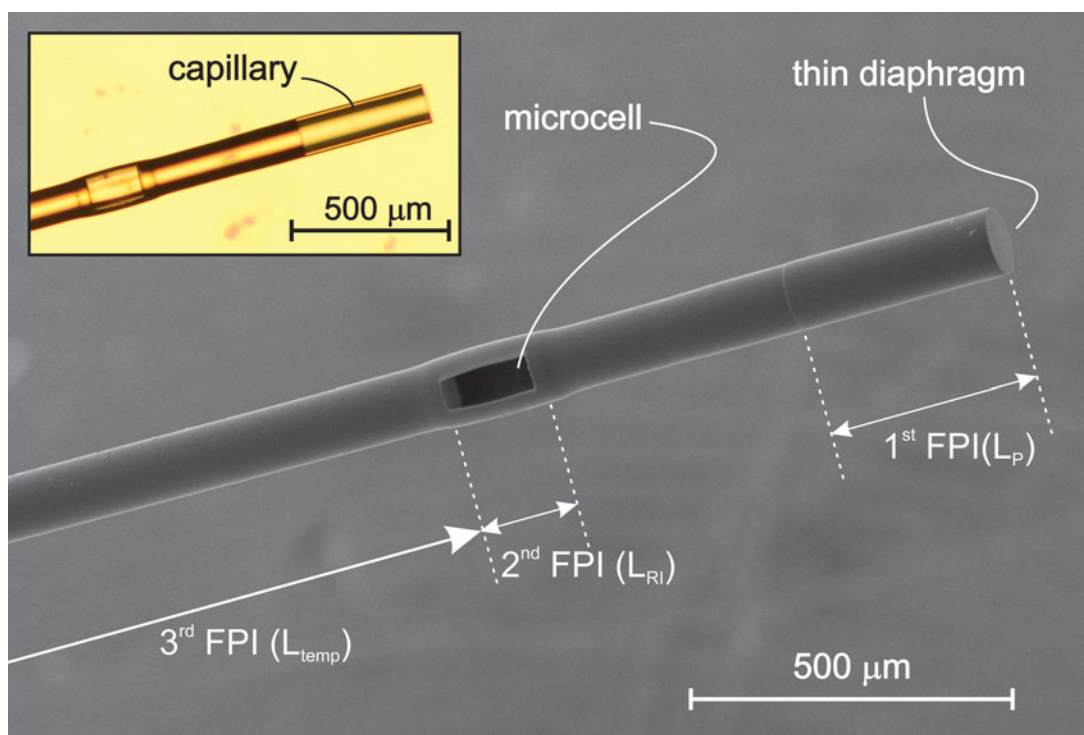 MultiParameter Fiber-Optic Sensor for Simultaneous Measurement of Thermal Conductivity, Pressure, Refractive Index, and Temperature

Simon Pevec
Denis Donlagic, *Member, IEEE*

IEEE

MultiParameter Fiber-Optic Sensor for Simultaneous Measurement of Thermal Conductivity, Pressure, Refractive Index, and Temperature

Simon Pevec and Denis Donlagic, *Member, IEEE*

Faculty of Electrical Engineering and Computer Science, University of Maribor, 2000 Maribor, Slovenia

Abstract: This paper presents a miniature, all-silica four/multiparameter sensor for simultaneous measurements of thermal conductivity, pressure, refractive index, and temperature of gases. The sensor is composed of multiple Fabry–Perot interferometers (FPIs) that were created at the tip of a standard optical fiber by a micromachining process based on selective etching and standard fiber manipulation steps. The experimental sensor length was below 3.4 mm, while the diameter did not exceed 125 μm. Interrogation of the sensor utilized acquisition and appropriate signal processing of the back-reflected optical spectrum, which allowed for crosstalk free extraction of individual resonators' lengths. High repeatability and resolutions were demonstrated for all four sensed parameters. The sensor might be applied to a variety of problems related to gas monitoring or composition analyze as, for example, binary, or even trinary gas mixtures.

Index Terms: Fabrication and characterization, fiber optics systems, advanced optics design, micro-optics, sensors.

1. Introduction

The rising complexity of industrial processes, bio-medical systems, and environmental monitoring methods often require sensing of more than one physical or chemical parameter. Furthermore, a harsh environment compatibility is often required in sensing systems that address gas measurements. This compatibility often includes chemical compatibility, broad temperature operational range, electromagnetic interference immunity, dielectric design, and explosion safety. Recent advances in micro-fluidic and micro-reactor systems also require miniaturization of available fluidic sensors' solutions. Miniaturization brings additional challenges in cases of small sensing devices designs, as those devices are more sensitive to oxidation and other degradation processes. Fiber-optic sensors can address many of the aforementioned challenges. Fiber-optic Fabry-Perot interferometers (FPIs) are one of the fiber sensing technologies [1], [2] that provide possibilities to build and design dual parameter sensors.

Reported examples of dual parameter sensors based on FPIs include, for example, sensors for simultaneous measuring of refractive index and temperature [3]–[7], sensors for simultaneous
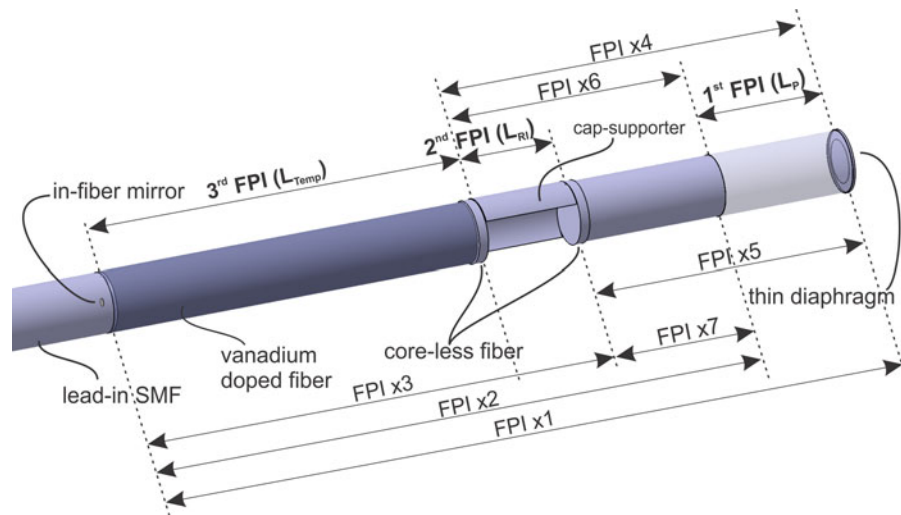
Fig. 1. Four parameter gas sensor design.

measurement of pressure and temperature [8]–[11], sensors for simultaneous measurement of strain and temperature [12], [13], sensors for simultaneous measurement of humidity and temperature [14], [15], and sensors for simultaneous measurements of pressure and refractive index [16], [17]. Many of those sensors feature an all silica design, which address compatibility with challenging environments and small size requirements successfully. There are only a few known solutions that provide the opportunity to sense more than two parameters [16], [18]–[22], but most of these solutions are either large in size and/or do not use an all-silica design or not allow simultaneous measurement of all parameters. Designing of a true, miniature, all-fiber, all-silica and compact sensor that can simultaneously sense more than two or more than three parameters with high resolution, while providing low crosstalk among individual parameters proved to be challenging.

In this paper, we present a four-parameter fiber-optic sensor for sensing of thermal conductivity pressure, refractive index and temperature of gases. The proposed sensor is created at the tip of an optical fiber and is less than 3.4 mm long. Pressure, refractive index, and temperature are very common parameters measured in different fluidic systems. Thermal conductivity is another interesting parameter that can provide valuable information on the gas state or composition. Currently, thermal conductivity is mostly limited to in-laboratory use; however, bringing this parameter into the field might provide additional and useful gas characterization opportunities.

2. Sensor Design and Operation

The presented sensor is shown in Fig. 1. The sensor utilizes three different FPIs stacked on the tip of a lead-in optical fiber for measurements of pressure, refractive index, temperature and thermal conductivity. Each FPI has a different length. This allows for spectral interrogation of the individual FPIs' lengths by application of the Inverse Fourier Transform (IFT) over the acquired optical spectrum as described in [5] and later in the Experimental section. The first FPI is made of a thin-wall glass capillary (OD/ID 125/85 μm) with a length of 390 μm and a flexible and thin silica diaphragm located on the top of the sensor structure. The diaphragm deflects proportionally to the absolute surrounding pressure and, thus, modulates the first FPI length. The second FPI is a 165 μm long open path U-shaped all-silica microcell, which allows for free access of the surrounding gas in-between the FPIs' semi-reflective surfaces and, thus, for gas RI measurements. A short section of Vanadium-Doped Fiber placed in between an in-fiber mirror and semi-reflective surface of the second FPI defines the third FPI. The length of the Vanadium-Doped Fiber corresponds to 2290 μm, while the distance between mirrors is slightly larger, i.e., 2320 μm, as the semi-reflective surface is separated

by a short segment of core-less fiber from the Vanadium-Doped Fiber due to reasons arising from the manufacturing process described further below. Vanadium doping induces high optical absorption at shorter wavelengths (i.e. 980 nm), while the increase in absorption near 1550 nm remains limited/low [23] In our particular case, we used fiber with absorption coefficients of about 159 dB/m at 980 and <8 dB/m at 1550 nm. This third FPI performs two functions: Temperature sensing and thermal conductivity measurement. Temperature is measured by observing the optical path length change of the third FPI, which is mainly temperature dependent due to the silica's refractive index dependence on the temperature (i.e. dn/dT fo silica corresponds to about 10^{-5} K^{-1}). On the other hand, the thermal conductivity is measured by application of active heating to this temperature sensitive segment. Active heating is achieved by application of a medium power 980 nm laser diode, which is coupled to the lead-in fiber in parallel with a signal integration system using a wavelength division multiplexing coupler. The 980 nm diode is turned on intermittently, until a new temperature steady state is achieved. The temperature change of the Vanadium-Doped Fiber caused by delivery of the known heating power to the fiber is then correlated to the thermal conductivity of the surrounding gas, as described in detail in the Signal Interrogation section. After measuring this temperature change, the heating laser is turned off, and the sensor segment returns quickly to the surrounding temperature.

Introduction of three FPIs along the single and short section of fiber also defines multiple cascaded semi-reflective surfaces, and combinations of these surfaces defined additional FPIs. In our particular design, seven additional FPIs can be identified along the proposed sensor as shown in Fig. 1. While these FPIs are not used for any sensing purpose, they modulate back-reflected optical spectrum with a distinctive set of spectral fringes (frequencies) and must be taken into account in sensor design to prevent overlap of spectral components that could cause crosstalk during signal readout. For example, none of the measurement FPI lengths shall coincide with any combination of sum lengths of any other FPIs, i.e. the first or the second or the third FPI lengths must not be equal or very similar to the sum of any other FPIs lengths.

3. Sensor Production Process

The sensor production process consists of multiple splice, cleave, etch and fiber or fiber sub-assembly manipulation steps. The entire process is shown in detail in Fig. 2.

The sensor production begins with stripping and cleaving a section of Vanadium-Doped Fiber (VDF). VDF is a single-mode fiber with germanium doped core that also contains small amounts of vanadium to create an absorbing single-mode fiber (more details on the fiber and its production can be found in [23]). The fiber tip is then immersed into Hydrofluoric Acid (HF) for 45 s. The doped region etches at a higher rate than pure silica, which results in a shallow cavity formation at the fiber tip (see Fig. 2(a)). This etched VDF is then spliced to a standard Single Mode lead-in Fiber SMF (see Fig. 2(b)) to create an in-fiber mirror (this technique for mirror production was described in detail in [24]). The VDF is then cleaved away from the splice/mirror at a distance that corresponds approximately to the third FPI length (see Fig. 2(c)). This completes the production of the first sensor's subassembly. The second subassembly production relates to a fabrication of the second (RI measuring) FPI. Here, we utilized a specially designed and produced Structure Forming Fiber (SFF) with a large and asymmetrically located phosphorus doped core as shown in Fig. 2(d) and discussed in detail in [5]. Phosphorus doped silica etches at a considerably higher rate than pure silica and can, thus, be removed selectively by the etching process [25] in proceeding manufacturing steps. The second subassembly preparation includes splicing of a short section of SFF in between two sections of coreless fiber (see Fig. 2(d)). The length of SFF defines approximately the length of the second (RI measuring) FPI. One of the coreless fibers is then precession-cleaved, about 30 μm from one of the splices (see Fig. 2(e)). This concludes preparation of the second subassembly. The first and the second subassemblies are further spliced together (the VDF fiber is spliced to a short coreless section) as shown in Fig 2(f). The protruding section of the coreless fiber is later cleaved about 30 μm away from the splice with the VDF, as depicted in Fig. 2(g). This concludes production of an intermediate sensor assembly. The third subassembly preparation relates to the pressure
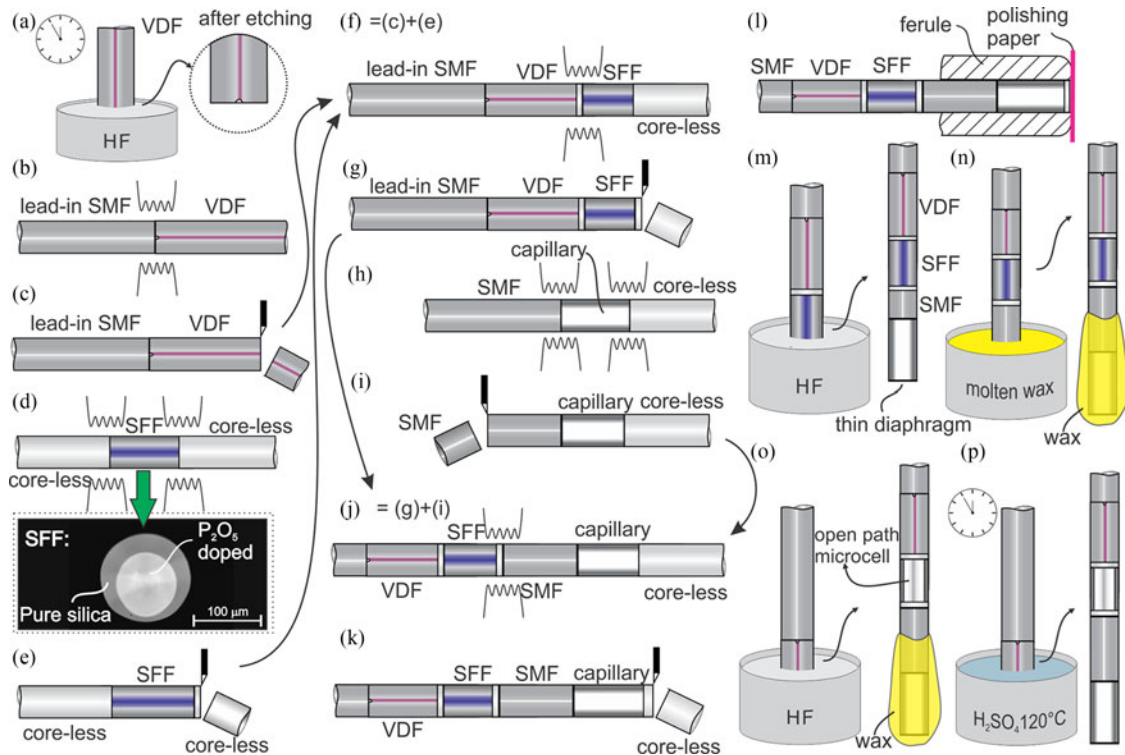
Fig. 2. Micromachining process for the production of a multiparameter FPIs sensor on the tip of an optical fiber.

sensing (first) FPI preparation and includes splicing a 390 μm long thin wall capillary in between a section of the SMF and the coreless fiber (see Fig. 2(h)). The capillary has an inner diameter of 85 μm and outer diameter of 125 μm. The SMF section is then trimmed to a distance that is less than 500 μm (see Fig. 2(i)), and this third subassembly is then spliced to the intermediate sensor assembly (consisting of the first and the second subassemblies) as represented by Fig. 2(j). The protruding section of coreless fiber is then converted into a pressure sensitive diaphragm. This is done by cleaving away the excess length of coreless fiber (see Fig. 2(k)), due to an even stress distribution near the fiber-to-capillary-splice, the cleave must be performed at least 50 μm away from the capillary-coreless fiber splice. The remaining coreless fiber is then polished to form an approximately 6 μm thick diaphragm on the tip of the sensor assembly (see Fig. 2(l)). While such polished diaphragm can already respond to a higher pressure, we further perform controlled etching to obtain a controllably thin and sensitive silica diaphragm (see Fig 2(m)). These steps conclude pressure sensor production. The described diaphragm forming process was adopted from the miniature pressure production process described in [26], [27]. After completion of the pressure sensor production, the pressure sensitive diaphragm is dipped briefly into the molten wax (see Fig. 2(n)) to provide temporary protection of the sensitive diaphragm during the final etching step in which we submerge the entire sensor into the HF for about 420 s to remove the phosphorus doped region of the SFF (see Fig. 2(o)), which is needed for the creation of the second (RI sensing) FPI. In the final step, the protective wax is removed by submersion of the entire sensor into hot sulfuric acid for few seconds (see Fig. 2(p)). The coreless fiber segments used at each side of the SFF are introduced to prevent damage to the surfaces of the VDF and SMF fibers during etching as the doped cores of both fibers etch at a higher rate in HF than the rest of the pure silica fiber cladding, which would otherwise reduce the surface reflectance if not protected by thin coreless sections. An example of the sensor produced by the above described procedure is shown in Fig. 3.
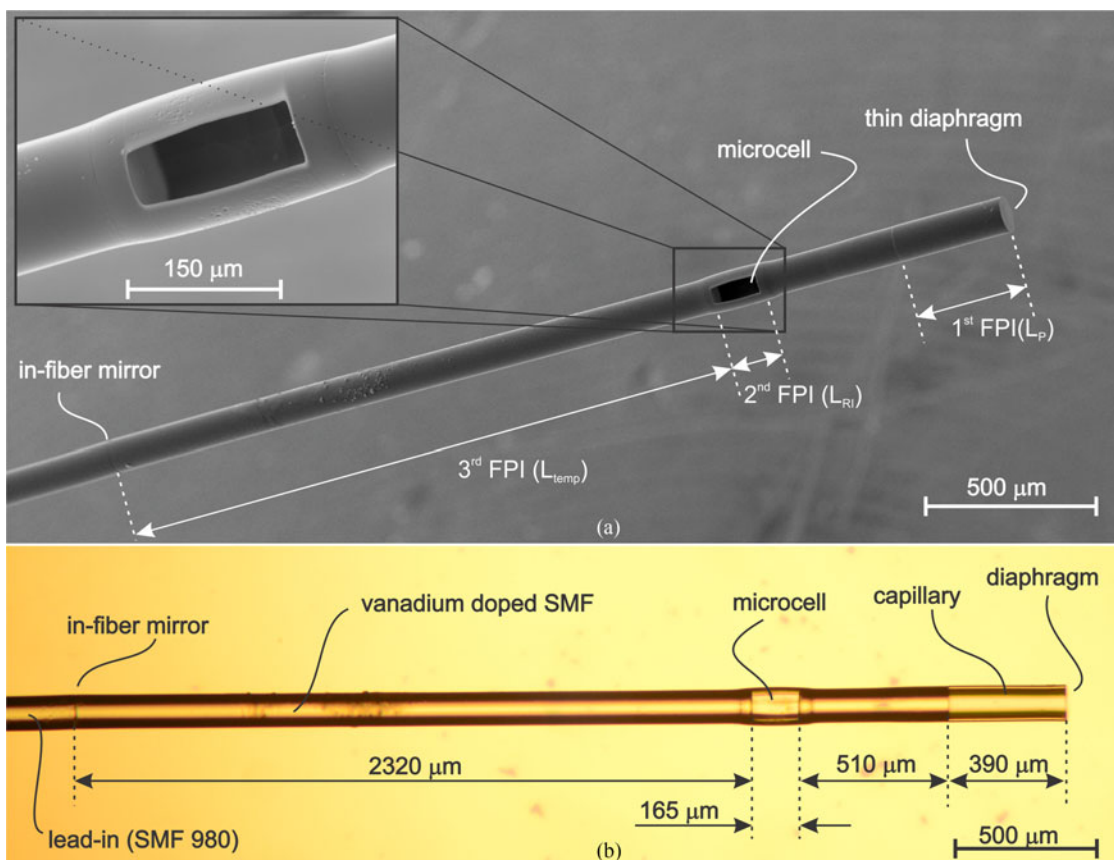
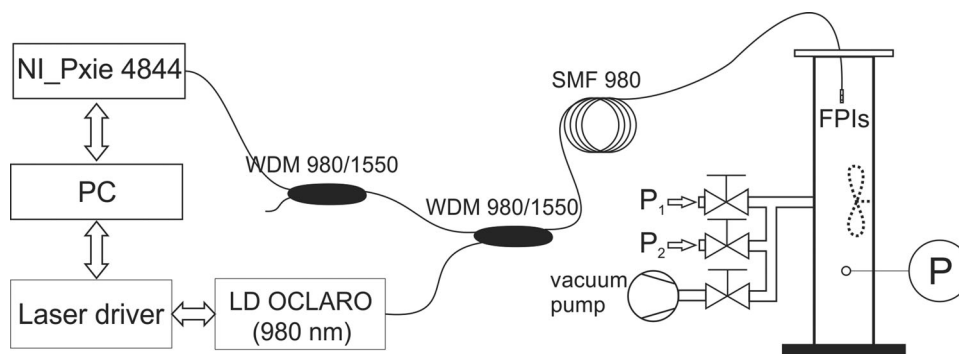Fig. 3. Fabricated sensor. (a) SEM image. (b) Optical image.

Fig. 4. Experimental setup.

4. Experimental Setup, Signal Processing, and Sensor Interrogation

The experimental measurement setup is shown in Fig. 4 and consisted of a National Instruments Pxie 4844 spectral interrogator, 980/1550 WDM couplers, a telecom 980 nm medium power laser diode source (the output power was feedback-stabilized to 50 mW) and a laser diode driver. The spectral interrogator and laser diode were controlled by a personal computer running custom Lab-View code. An additional 980/1550 WDM coupler was used to improve isolation between the 1550 nm signal and 980 heating wavelengths. The sensor was mounted into a steel vessel with
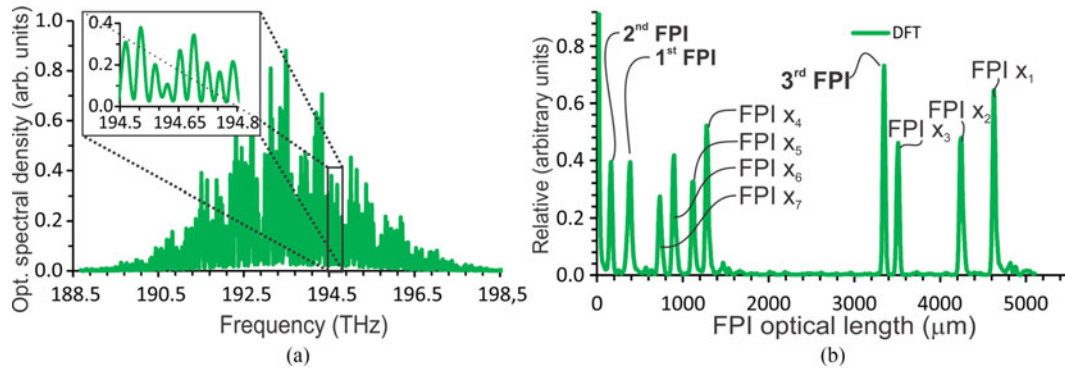
Fig. 5. Sensor's back-reflected optical spectrum with applied Gaussian window. (b) IFT of optical spectrum where the x-axes are multiplied by c/2.

a volume of about $1.6\,dm^3$. The vessel was also equipped with a small fan which promoted gas mixing (the sensor was however shielded from direct gas flow over the sensor). The vessel was equipped with a vacuum pump, reference pressure sensor, range of valves that allowed test gas delivery and venting valve connected to the vessel over a long and thin tube, which was used to bring the vessel to the normal atmosphere pressure during the testing. Gas mixing was performed by adjusting partial pressures of individual gas components (the chamber was always evacuated prior to any test, and then partial pressures of the gases in the mixture were set by controlling valves connected to high pressure pure gas cylinders; after the mixing the vessel was always above the normal pressure, and the vent valve was used to bring the vessel to a nominal pressure when so required by the measurement).

To measure individual FPIs' lengths we acquired the sensor's back-reflected optical spectra within the range from 188.5 THz to 198.5 THz (i.e., from 1510 to 1590 nm). After applying a Gaussian window to the acquired spectra, we calculated its Inverse Fourier Transform (IFT). The magnitude of IFT contains peaks at positions that correspond to individual FPIs' lengths (the x-axis of IFT actually represents times of flight in-between resonators' mirrors; thus, to obtain optical distances among mirror pairs, the x-axis of the IFT is multiplied by c/2). An example of acquired spectra and its magnitude IFT are shown in Fig. 5(a) and (b) respectively. One can recognize ten peaks which correspond to FPIs' lengths also shown in the Fig. 1. The peaks belonging to the first, second, and the third FPI were used further to perform sensor interrogation.

To measure small changes in the *OPL* of individual sensing FPIs, we utilize phase tracking of corresponding spectral fringes in the acquired optical spectrum [5]. Thus, phase components of the IFT ($\angle$IFT) that correspond to sensing FPIs' lengths were calculated and correlated to the Optical Path-Length (*OPL*) changes (i.e., phases of components that correspond to the sensing FPIs' peak locations in the magnitude of IFT):

$$\Delta OPL_X = \lambda \frac{\Delta\varphi}{2\pi} = \lambda \frac{\angle \text{IFT}\left(\frac{2}{c}L_{FPI\_X}\right)}{2\pi} \tag{1}$$

where index *X* indicates a particular FPI (in reference to Fig. 1, *X* would be 1 for pressure, 2 for *RI* and 3 for temperature/*VDF FPI*) and λ is a central wavelength. This approach provides an efficient way for low-cross-talk readout of individual FPI lengths' changes from complex interference spectra generated by multiple cavities. Individual parameters were then calculated as:

Pressure was calculated as:

$$p = p_0 + \frac{1}{k_P}\Delta OPL_{1stFPI}$$

$$= p_0 + \frac{1}{k_P}\frac{\lambda}{2\pi}\Delta\varphi_{1st\_FPI} \tag{2}$$

where p_0 is initial pressure at calibration, and k_p is the diaphragm's pressure sensitivity, which is obtained either during the production process or by separate calibration after pressure sensor production (i.e. using a two-point calibration process, for example, at $p = 0$ and $p = 1$ Bar). A typical value for k_p, obtained after the controlled etching process of the diaphragm, was -183 nm/bar.

RI was calculated as

$$
\begin{aligned}
\text{RI} &= n_0 + \frac{\Delta OPL_{2^{nd}FPI}}{2L_{2^{nd}\_FPI}} \\
&= n_0 + \frac{\lambda}{2L_{2^{nd}\_FPI} \cdot 2\pi} \Delta\varphi_{2^{nd}\_FPI}
\end{aligned}
\tag{3}
$$

where n_0 is the initial RI at calibration. Since the RI of gas is also pressure sensitive, the RI measurement can be compensated for pressure changes using data obtained from the pressure sensing FPI (this is important when gas composition is anticipated from the RI measurement). Pressure compensated RI value (RI_{PC}) can be calculated as

$$
\begin{aligned}
\text{RI}_{PC} &= n_0 + \left(\Delta\varphi_{2^{nd}\_FPI} - \frac{1}{k_P} \frac{\lambda}{2\pi} \Delta\varphi_{1^{st}\_FPI} \cdot k_{RI\_P} \right) \\
&\quad \cdot \frac{\lambda}{2L_{2^{nd}\_FPI} \cdot 2\pi} \circ
\end{aligned}
\tag{4}
$$

where k_{RI_P} presents the refractive index pressure correction constant, which is obtained by calibration, i.e. by measuring phase change or *OPL* change of the second FPI when applying a known calibrate pressure change.

Temperature was calculated as

$$
\begin{aligned}
T &= T_0 + \frac{\Delta OPL_{1^{st}FPI}}{2L_{3^{rd}\_FPI} \cdot \frac{dn}{dT}(SiO_2)} \\
&= T_0 + \frac{\lambda}{2L_{3^{rd}\_FPI} \cdot \frac{dn}{dT}(SiO_2) \cdot 2\pi} \circ \Delta\varphi_{3^{rd}\_FPI}
\end{aligned}
\tag{5}
$$

where T_0 is the initial temperature obtained during calibration at known temperature.

The thermal conductivity measurement was accomplished by turning ON and OFF the 980 nm medium-power laser diode, which periodically heated the *VDF* that constitutes the third FPI. The ON and OFF cycles must have a sufficient duration (typically 5 *s*) to allow for the *VDF*'s temperature to achieve steady state value. The time that needs to lapse between laser activation and deactivation is governed by the fiber's time constant, which corresponds to about 400 *ms* in air [23]. During the diode's ON-cycle, the diode's output power was also stabilized with the help of the closed-loop control to 50 mW. The periodic changes in VDF temperature modulate the *OPL* of the third FPI, which can be further correlated directly to the thermal conductivity of the surrounding gas as in [23]

$$
\Delta OPL_{3^{rd}\_FPI} = P_A \frac{1}{\pi} \left(n \frac{dn}{dT} \right) \frac{1}{Nuk_f}
\tag{6}
$$

where P_A represents the total absorbed optical power by the *VDF*, k_f is the thermal conductivity of the gas surrounding the sensor, n the silica refractive index, *dn/dT* the change of fiber refractive index due to temperature change, and *Nu* is the Nusselt number. The Nusselt number is a semi-empiric fluid-dynamic parameter. There are different expressions available in the literature for its calculation such as, for example, [28] $Nu = (0.6 + 387 \times Ra^{1/6}/(1 + (0.559/Pr)^{9/16})^{8/27}$, where *Pr*, and *Ra* are Prandtl and Rayleigh numbers respectively, which are further defined as $Pr = \mu_f c_f / k_f$ and $Ra = Gr \times Pr$, where *Gr* represents the Grashof number $Gr = 8b^3 \rho_f^2 g \Delta T \beta_f$, and where $2b$ represents the fiber diameter, ρ_f surrounding gas density, g gravitational acceleration, ΔT the temperature difference between the surrounding gas and the fiber surface, β_f the surrounding gas thermal expansion coefficient, μ_f the surrounding gas viscosity, and c_f the surrounding gas specific heat. The Nusselt number can, however, be considered constant in many cases, especially when applying the sensor to similar gases [29].
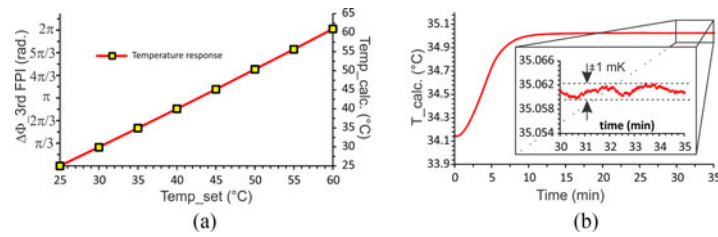
Fig. 6. (a) Sensor's response to temperature change. (b) Response of the third interferometer to show temperature resolution (a moving average of 400 samples was used).
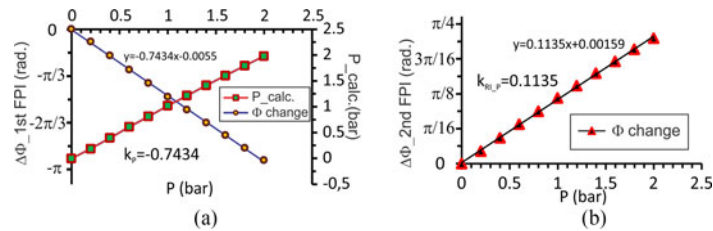

Fig. 7. Sensor's response to pressure change. (a) Response of first FPI related to the displacement of the thin diaphragm on the sensor tip. (b) Response of second FPI related to the pressure induced RI change of the gas.

Finally, since the parameters in the above expressions can be determined with limited certainty (the expressions are valid for infinitely long cylindrical bodies, the determination of absolute absorbed power is uncertain; expressions for Nusselt number determination might have limited accuracy for small bodies as is the case in the present sensor) the expression 6 can be rewritten in the form

$$k_f = \frac{c_0}{\Delta OPL_{3^{rd}\_FPI}} \tag{7}$$

where c_o is a calibration constant that can be estimated in a calibration process using pure and known gas with known k_f.

5. Experimental Results

In this section gas temperature, pressure and compositions were changed to demonstrate the capability for independent measurements of all four parameters. Fig. 6 shows the sensor's temperature response. Fig. 6(a) shows the third FPI's phase change and corresponding temperature, calculated according to (5), when the sensor's temperature is changed between 25 and 60 °C. Initial (zero) calibration of the senor was performed at 25 °C. As expected, we obtained a well-defined linear response. Fig. 6(b) demonstrates the resolution that can be achieved by the presented sensor and proposed signal interrogation. The sensor temperature was changed by about 1 $C°$, while output stability and fluctuation of the signal was observed for 30 min. The output signal was filtered digitally by moving average filter (400 samples) while the original sampling rate of NI Pxie 4844 spectral integrator was 10 Hz. The absolute output noise peak-to-peak amplitude corresponded to about 2 mK, which also indicates the achievable resolution of the sensor in the presented setup.

Fig. 7 depicts the response of the sensor to the pressure change. Fig. 7(a) shows the first FPI phase change together with calculated pressure (phase change of the first FPI was converted into the pressure using (2) and initial calibration at 0 bar). A linear response was obtained with pressure sensitivity of −0.743 rad/bar (equivalent to −183 nm/bar of diaphragm displacement). Pressure change of the gas has, however, also a profound effect on the RI of the same gas, which is shown in
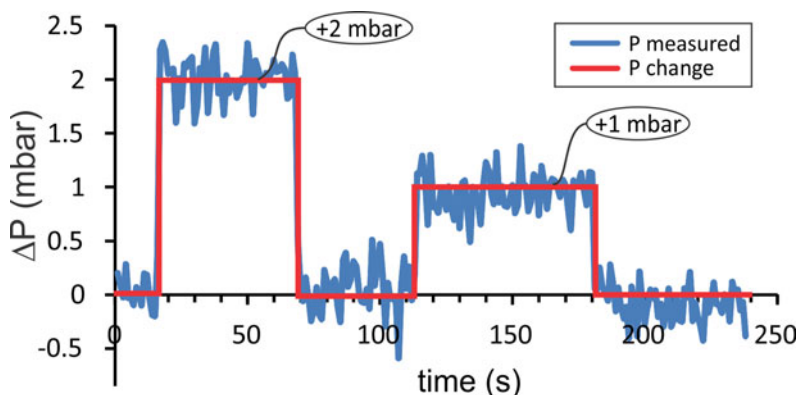
Fig. 8. Response of first interferometer to show the sensor's pressure resolution.
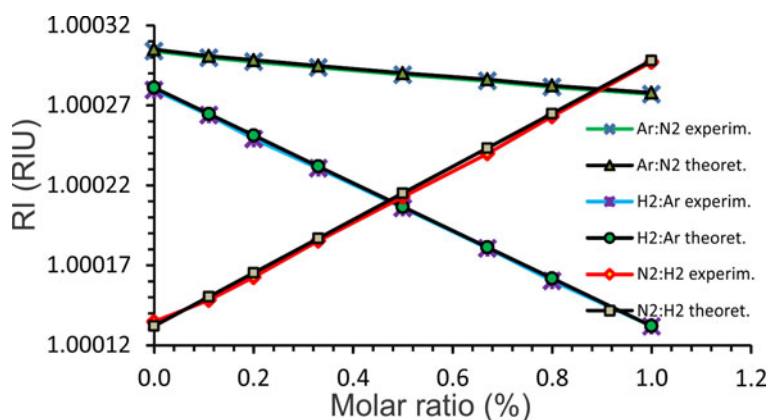

Fig. 9. Response of second FPI to measure RI of three different binary mixtures; experimental results are compared with calculations based on a simple proportional Arago-Biot equation.

Fig 7(b). This data was used further in RI sensing to compensate for pressure induced RI changes (compensation factor k_{RI_P}, required for compensation was also calculated during this test).

Fig. 8 demonstrates the responses of the sensor to small changes in pressure. The results indicate that the produced sensor, interrogated by the proposed IFT algorithm, was able to resolve pressure changes as small as 1 mBar (peak-to-peak noise amplitude corresponded to about 0.5 mBar).

In the following series of tests we evaluated the RI sensing capability of the proposed sensor. For this purpose, we prepared different gas mixtures (argon-nitrogen, argon-hydrogen and helium-nitrogen) with different molar concentrations of gases. All measurements were performed at normal pressure. Initial (zero calibration) was obtained by using pure gases at normal pressure. Fig. 9 shows RIU change during gas composition variation (RIU was calculated from the second FPI phase change using (3)). For comparison, we added RI data/curves for the used mixtures, calculated from the gas molar ratios and known RI of pure gases [30]. As expected, linear responses were obtained between the RI of gases' mixtures molar ratio and the values calculated by (3).

To demonstrate the sensor's RIU resolution, we filled our test vessel with air and then we injected into the same vessel small volumes of hydrogen gas in three consecutive steps, which caused step-decreases of RI of the gas mixture (in a total volume of about 1.6 dm^3, we injected 5 cm^3 of hydrogen gas consecutively three times). A small electric fan was placed into the test vessel to promote gas mixing. Injections of hydrogen gas also caused small pressure changes. All these steps are visible in the recorded responses. Fig. 10(a) shows the phase change obtained for the second (RI measuring FPI). The injection of gas increased the pressure within the vessel, which
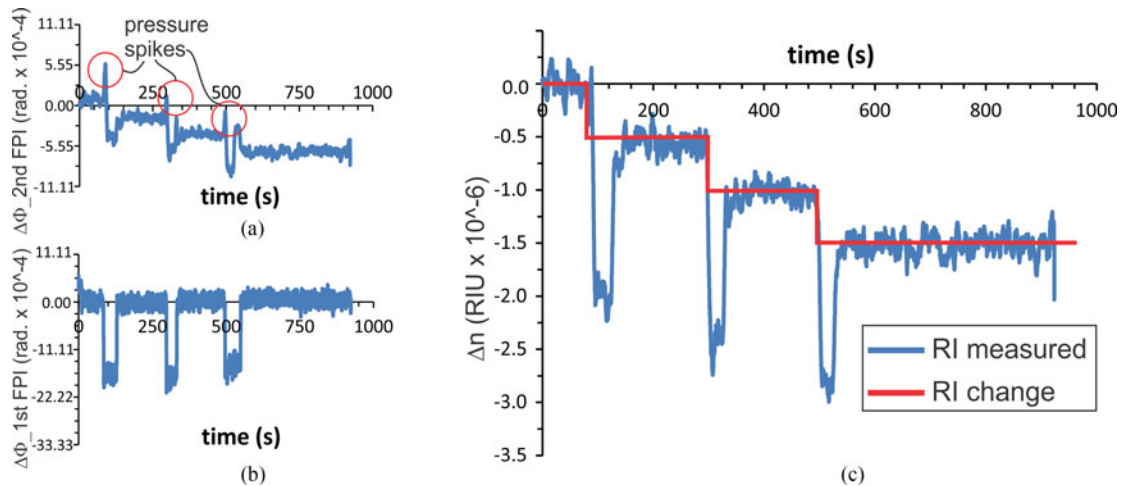
Fig. 10. (a) "Raw" response of the second FPI during the gas injection test. (b) Response of the first FPI during the gas injection test. (c) Pressure compensated RI response showing RI resolution and successful pressure compensation during the gas injection test.
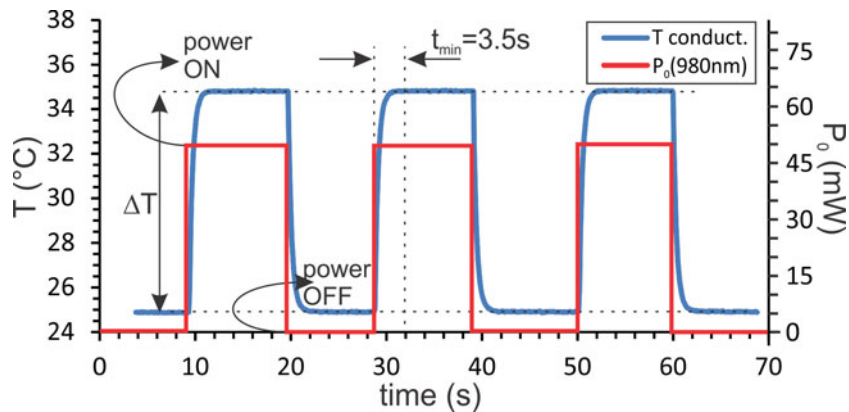

Fig. 11. Response of third FPI during thermal conductivity measurements; the sensor was exposed to a pure N_2 atmosphere.

resulted in the response of the first and the second FPIs (see Fig. 10(b)). The net change of the gas RI instantly after injection was positive (pressure increased, but gas mixing did not occur instantly), thus causing a transient increase in the RI of the gas in the cylinder (spikes in Fig. 10(a)). Immediately after gas injection we also performed pressure equalization with the surroundings (returning the vessel to the nominal pressure). Since the injection occurred near the sensor and since the RI of the injected gas was lower that the initial base gas (air) RI in the vessel, the transient increase in second FPI phase was followed by a stronger phase drop. After full mixing of the gases was completed the second FPI phase stabilized at equilibrium level. Finally, Fig. 10(c), shows a fully compensated (pressure independent) RI measurement calculated from (4) and raw data obtained from the first and the second FPI.

Fig. 10(c) indicates successful compensation of the pressure influence (the remaining downward pointing spikes are due to the actual fluctuations of gas during the mixing process), while demonstrating an RI resolution of about 5×10^{-7} RIU.

The last series of tests was dedicated to the measurement of the thermal conductivity. Fig. 11 shows the response of the third (temperature sensing) FPI when the laser diode is switched ON
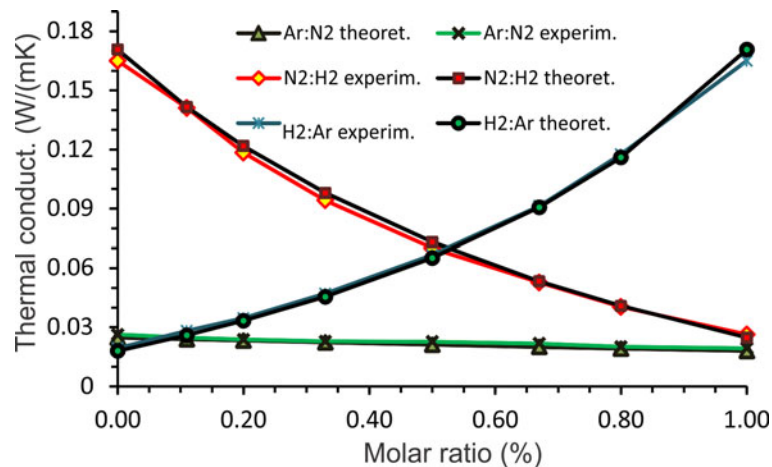
Fig. 12. Thermal conductivity obtained from measured temperature variation of the third FPI during cyclical application of the 980 nm heating power. For comparison, the calculated thermal conductivity of the binary mixtures is also shown.

and OFF. The temperature change of about 10 K was obtained in nitrogen when using a 50 mW output power 980 nm laser diode. The cycle to cycle temperature change was stable and repeatable. The temperature difference measurement was always performed about 3.5 s after excitation diode toggling, to allow full transition to a steady-state even in the case of less thermally conductive gases.

The thermal conductivity was calculated according to (7) while performing initial calibration using Hydrogen. Different gas mixtures with different gas molar ratios were then used to observe the sensor's response as shown in Fig. 12. Molar gas ratio and thermal conductivity are not in a linear relation (as opposed to RI, which is in a linear relationship with molar gas ratio). For the reference we calculated and added in the Fig. 12 theoretically predicted values for the used binary mixtures. We used theoretical model provided in ref. [31].

The results indicated good agreement between the measured and anticipated thermal conductivities of the different gas mixtures and the possibility to distinguish even among gases with very similar thermal conductivities, as for example argon and nitrogen.

Finally, crosstalk analysis among individual sensors' measurement parameters was performed. Pressure and temperature are parameters, which are independent of the sensed gas physical properties/composition, and can be thus determined straightforwardly. In this experiment we firstly kept the sensor at the room temperature (which can be considered constant for short period of time), while we varied surrounding's gas pressure and refractive index over typical sensor's operation range, i.e. pressure was changed from −1 bar to 2.5 bar, and the RI was changed from 1.00013 to 1.0003 RIU. Results are shown in Fig. 13. These changes in RI and pressure caused fluctuations in the sensor's temperature read-out of less than 0.03 °C, which was within the range of the sensors' temperature setting uncertainty (gas injection and pressure fluctuation also caused the temperature fluctuations within the test vessel and the sensor temperature stability better than 0.05 °C was difficult to guarantee in this experiment). Thus, the cross-sensitivity of the pressure and RI to the sensor's temperature readout can be considered negligible.

Similar experiment was also provided to demonstrate impact of RI and temperature variation onto the pressure read-out. In this experiment, the sensor was keep at constant pressure of 0 bar (atmospheric pressure), while we varied RI and temperature as shown in Fig. 14. The RI change between 1.00013 to 1.0003 RIU caused change in the pressure read-out of less than 1 mBar, which can be also considered as negligible and within the range of sensor's pressure measurement resolution. The temperature induced change in the pressure red-out was, however, higher and corresponded to about 2.9 mBar/K as shown in Fig. 14(b). This result is predictable and repeatable
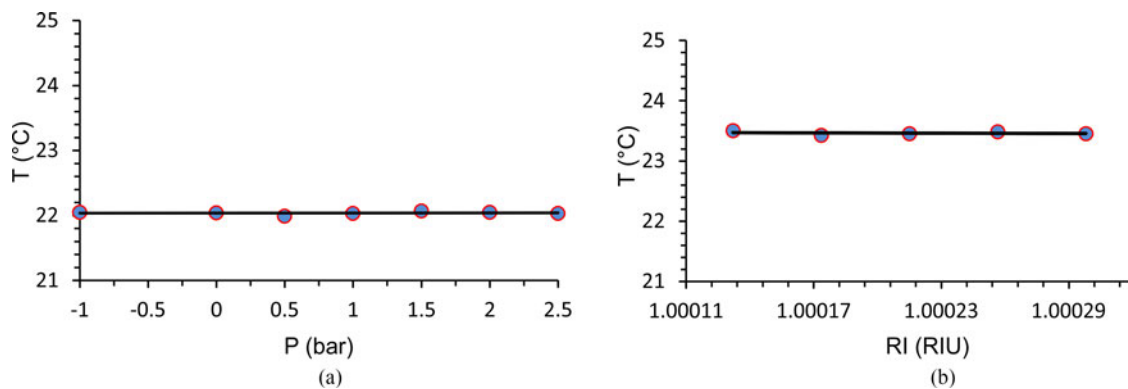
Fig. 13. Temperature cross-sensitivity to (a) pressure and (b) refractive index.
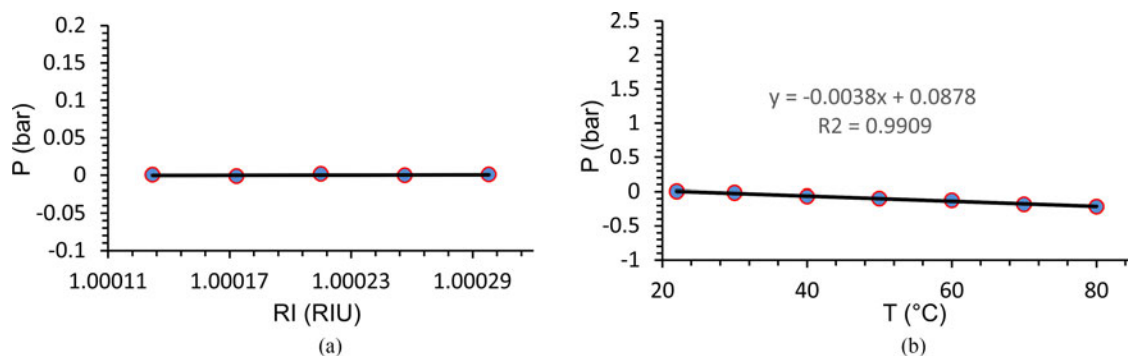

Fig. 14. Pressure cross-sensitivity to (a) refractive index and (b) temperature.

and can be thus compensated by using data from the temperature sensor. This pressure cross-sensitivity to temperature can be mainly contributed to the thermal expansion of the sensor's pressure measurement cavity and pressure change within the same cavity as it was already studied for similar types of sensors (example in [26]).

RI and the thermal conductivity of a particular gas, on the other hand, exhibits strong intrinsic dependence on pressure and temperature. Thus, the direct determination of sensor's intrinsic cross sensitivity of RI measurement to other parameters proves to be more complex. However, since previous two experiments clearly show that the particular cavity's length readout is independent of any other cavity length, it can be concluded that intrinsic RI measurement crosstalk to other parameters shall be small and that dependence of RI on pressure and temperature predominantly arise from intrinsic gas interrelations among those parameters. When pressure and/or temperature independent RI readout is required for the case of a particular gas, a calibration procedure can be implemented as shown above for the case of air. Similarly, temperature independent RI readout can be obtained through similar calibration process, as for example described in [5] or in other similar references. Finally, the thermal conductivity, which is measured through above described opto-fluido-dynamic effect, relies on measurements of sensor's temperature change under active heating. Since the temperature readout is fully independent from measurement of any other parameter, no intrinsic sensor's crosstalk between thermal conductivity read-out and other measured parameters can be expected. Certainly, thermal conductivity of particular gas by-it-self depends on pressure and temperature, but those relationships are intrinsic properties of measured gas and not the sensor itself.

6. Conclusion

This paper presented a multi-parameter (four) parameter sensor, which can measure pressure, refractive index, temperature and thermal conductivity of gases simultaneously. The sensor is composed of multiple FPI resonators that were created and cascaded at the tip of a standard optical fiber. The total experimental sensor length did not exceed 3.4 mm, while the diameter was the same as the diameter of a standard optical fiber (125 μm). The sensor was produced by a micromachining process based on a sequence of splice, cleave and etching operations. The production process utilized standard fiber handling equipment, while two different special fibers were used to produce an RI measuring microcell and optically heatable temperature sensor. Interrogation of the sensor was based on the acquisition of the back-reflected sensor's optical spectrum, which was processed further by an IFT based algorithm to extract phases of the spectral fringes belonging to the measurement FPIs. These phases were correlated further to individual FPIs' optical path length changes. No significant cross-talk was observed among the extracted path lengths of individual FPIs.

High repeatability and resolutions were demonstrated for all four sensed parameters (a temperature resolution of 2 mK, pressure resolution of 1 mBar, RI resolution of 5×10^{-7} RIU and thermal conductivity of better than 1×10^{-3} W/mK were achieved). The sensor also allows for correction/compensation of gas RI measurements due to the pressure changes. Temperature compensation can be also introduced easily when/if required in RI or other parameters' measurements.

The proposed sensor might be applied to a variety of problems related to gas monitoring or composition analyze such as, for example, binary or even trinary gas mixtures. Its small size allows for characterization of small gas volumes, while its all silica design provides compatibility with high temperatures and/or chemically harsh environments.

Acknowledgment

References

[1] E. Udd, *Fiber Optic Smart Structures*, New York, NY, USA: Wiley, 1995, pp. 249–269.
[2] T. Zhu, D. Wu, M. Liu, and D. W. Duan, "In-line fiber optic interferometric sensors in single-mode fibers," *Sensors*, vol. 12, no. 8, pp. 10430–10449, Aug. 2012.
[3] R. H. Wang and X. G. Qiao, "Hybrid optical fiber Fabry-Perot interferometer for simultaneous measurement of gas refractive index and temperature," *Appl. Opt.*, vol. 53, no. 32, pp. 7724–7728, Nov. 2014.
[4] X. L. Tan *et al.*, "UV-curable polymer microhemisphere-based fiber-optic Fabry-Perot interferometer for simultaneous measurement of refractive index and temperature," *IEEE Photon. J.*, vol. 6, no. 4, Aug. 2014, Art. no. 7800208.
[5] S. Pevec and D. Donlagic, "High resolution, all-fiber, micro-machined sensor for simultaneous measurement of refractive index and temperature," *Opt. Exp.*, vol. 22, no. 13, pp. 16241–16253, Jun. 2014.
[6] T. T. Wang and M. Wang, "Fabry-Perot fiber sensor for simultaneous measurement of refractive index and temperature based on an in-fiber ellipsoidal cavity," *IEEE Photon. Tech. Lett.*, vol. 24, no. 19, pp. 1733–1736, Oct. 2012.
[7] D. W. Kim, F. Shen, X. P. Chen, and A. B. Wang, "Simultaneous measurement of refractive index and temperature based on a reflection-mode long-period grating and an intrinsic Fabry-Perot interferometer sensor," *Opt. Lett.*, vol. 30, no. 22, pp. 3000–3002, Nov. 2005.
[8] Y. A. Zhang, J. Huang, X. W. Lan, L. Yuan, and H. Xiao, "Simultaneous measurement of temperature and pressure with cascaded extrinsic Fabry-Perot interferometer and intrinsic Fabry-Perot interferometer sensors," *Opt. Eng.*, vol. 53, no. 6, Jun. 2014, Art. no. 067101.
[9] S. Pevec and D. Donlagic, "Miniature all-fiber Fabry-Perot sensor for simultaneous measurement of pressure and temperature," *Appl. Opt.*, vol. 51, no. 19, pp. 4536–4541, Jul. 2012.
[10] K. Bremer *et al.*, "Feedback stabilized interrogation technique for EFPI/FBG hybrid fiber-optic pressure and temperature sensors," *IEEE Sensors J.*, vol. 12, no. 1, pp. 133–138, Jan. 2012.
[11] P. Morris, A. Hurrell, A. Shaw, E. Zhang, and P. Beard, "A Fabry-Perot fiber-optic ultrasonic hydrophone for the simultaneous measurement of temperature and acoustic pressure," *J. Acoustical Soc. Amer.*, vol. 125, no. 6, pp. 3611–3622, Jun. 2009.
[12] T. Geng *et al.*, "Modal interferometer using three-core fiber for simultaneous measurement strain and temperature," *IEEE Phot. J.*, vol. 8, no. 4, Aug. 2016, Art. no. 6803908.
[13] Y. H. Pan *et al.*, "Simultaneous measurement of temperature and strain using spheroidal-cavity-overlapped FBG," *IEEE Phot. J.*, vol. 7, no. 6, Dec. 2015, Art. no. 6803406.

[14] S. Pevec and D. Donlagic, "Miniature all-silica fiber-optic sensor for simultaneous measurement of relative humidity and temperature," *Opt. Lett.*, vol. 40, no. 23, pp. 5646–5649, Dec. 2015.

[15] S. N. Wu *et al.*, "An open-cavity Fabry-Perot interferometer with PVA coating for simultaneous measurement of relative humidity and temperature," *Sensors Actuators B-Chem.*, vol. 225, pp. 50–56, Mar. 2016.

[16] R. D. Pechstedt, "Fibre optical sensor for simultaneous measurement of pressure, temperature and refractive index," in *Proc. 23rd Int. Conf. Opt. Fibre Sensors*, 2014, vol. 9157, pp. 91570I-1–91570I-4.

[17] S. Pevec and D. Donlagic, "Miniature fiber-optic sensor for simultaneous measurement of pressure and refractive index," *Opt. Lett.*, vol. 39, no. 21, pp. 6221–6224, Nov. 2014.

[18] X. Wang, S. Q. Lou, X. Z. Sheng, and S. Liang, "Simultaneous measurement of torsion, strain and temperature using a side-leakage photonic crystal fiber loop mirror," *Infrared Phys. Technol.*, vol. 76, pp. 603–607, May 2016.

[19] N. J. Alberto, C. A. Marques, J. L. Pinto, and R. N. Nogueira, "Three-parameter optical fiber sensor based on a tilted fiber Bragg grating," *Appl. Opt.*, vol. 49, no. 31, pp. 6085–6091, Nov. 2010.

[20] X. K. Zeng and Y. J. Rao, "Simultaneous static strain, temperature and vibration measurement using an integrated FBG/EFPI sensor," *Chin. Phys. Lett.*, vol. 18, no. 12, pp. 1617–1619, Dec. 2001.

[21] D. Jauregui-Vazquez *et al.*, "Modified all-fiber Fabry-Perot interferometer and its refractive index, load, and temperature analyses," *IEEE Phot. J.*, vol. 7, no. 3, Jun. 2015, Art. no. 6600109.

[22] R. Oliveira *et al.*, "Simultaneous measurement of strain, temperature and refractive index based on multimode interference, fiber tapering and fiber Bragg gratings," *Meas. Sci. Technol.*, vol. 27, no. 7, Jul. 2016, Art. no. 075107.

[23] Z. Matjasec, S. Campelj, and D. Donlagic, "All-optical, thermo-optical path length modulation based on the vanadium-doped fibers," *Opt. Exp.*, vol. 21, no. 10, pp. 11794–11807, May 2013.

[24] E. Cibula and D. Donlagic, "Low-loss semi-reflective in-fiber mirrors," *Opt. Exp.*, vol. 18, no. 11, pp. 12017–12026, May 2010.

[25] S. Pevec, E. Cibula, B. Lenardic, and D. Donlagic, "Micromachining of optical fibers using selective etching based on phosphorus pentoxide doping," *IEEE Photon. J.*, vol. 3, no. 4, pp. 627–632, Aug. 2011.

[26] D. Donlagic and E. Cibula, "All-fiber high-sensitivity pressure sensor with SiO2 diaphragm," *Opt. Lett.*, vol. 30, no. 16, pp. 2071–2073, Aug. 2005.

[27] E. Cibula, S. Pevec, B. Lenardic, E. Pinet, and D. Donlagic, "Miniature all-glass robust pressure sensor," *Opt. Exp.*, vol. 17, no. 7, pp. 5098–5106, Mar. 2009.

[28] F. P. Incropera, D. P. Dewitt, T. L. Bergman, and A. S. Lavine, *Fundamentals of Heat and Mass Transfer*, 6th ed. Hoboken, NJ, USA: Wiley, 2007.

[29] W. H. Lipkea and G. S. Springer, "Heat transfer through gases contained between two vertical cylinders at different temperatures," *Int. J. Heat Mass Trans.*, vol. 11, pp. 1341–1350, 1968.

[30] D. F. J. Arago and J. B. Biot, *Mem. Acad. Fr.*, pp. 7–11, 1806.

[31] S. R. Prajapati and J. D. Pandey, "Thermal conductivities and viscosities of some binary and ternary monoatomic gas mixtures," *Chem. Phys.*, vol. 4, pp. 428–434, 1981.